



HAL
open science

Cyclic oxidation of coated and uncoated single-crystal nickel-based superalloy MC2 analyzed by continuous thermogravimetry analysis

Aymeric Raffaitin, Daniel Monceau, Eric Andrieu, Fabrice Crabos

► To cite this version:

Aymeric Raffaitin, Daniel Monceau, Eric Andrieu, Fabrice Crabos. Cyclic oxidation of coated and uncoated single-crystal nickel-based superalloy MC2 analyzed by continuous thermogravimetry analysis. *Acta Materialia*, 2006, 54 (17), pp.4473-4487. 10.1016/j.actamat.2006.05.034 . hal-03597267

HAL Id: hal-03597267

<https://hal.science/hal-03597267>

Submitted on 4 Mar 2022

HAL is a multi-disciplinary open access archive for the deposit and dissemination of scientific research documents, whether they are published or not. The documents may come from teaching and research institutions in France or abroad, or from public or private research centers.

L'archive ouverte pluridisciplinaire **HAL**, est destinée au dépôt et à la diffusion de documents scientifiques de niveau recherche, publiés ou non, émanant des établissements d'enseignement et de recherche français ou étrangers, des laboratoires publics ou privés.



Open Archive Toulouse Archive Ouverte (OATAO)

OATAO is an open access repository that collects the work of Toulouse researchers and makes it freely available over the web where possible.

This is an author-deposited version published in: <http://oatao.univ-toulouse.fr/>
Eprints ID : 2525

To link to this article :

URL : <http://dx.doi.org/10.1016/j.actamat.2006.05.034>

To cite this version : Raffaitin, Aymeric and Monceau, Daniel and Andrieu, Eric and Crabos, Fabrice (2006) [*Cyclic oxidation of coated and uncoated single-crystal nickel-based superalloy MC2 analyzed by continuous thermogravimetry analysis.*](#) Acta Materialia, vol. 54 (n° 17). pp. 4473-4487. ISSN 1359-6454

Any correspondence concerning this service should be sent to the repository administrator: staff-oatao@inp-toulouse.fr

Cyclic oxidation of coated and uncoated single-crystal nickel-based superalloy MC2 analyzed by continuous thermogravimetry analysis

A. Raffaitin ^{a,b}, D. Monceau ^{a,*}, E. Andrieu ^a, F. Crabos ^b

^a CIRIMAT UMR 5085 (INPT/UPS/CNRS), ENSIACET, 31077 Toulouse, France

^b TURBOMECA-SAFRAN, 64511 Bordes, France

Abstract

The previously developed cyclic thermogravimetry analysis (CTGA) [Monceau D, Poquillon D. Oxid Met 2004;61:143–163] method is applied to the cyclic oxidation at 1150 °C of a NiCoCrAlYTa-coated and an uncoated single-crystal nickel-based superalloy MC2. A new procedure to correct the buoyancy effect is proposed in order to evaluate the amount of oxide formed during the heating periods, which can be important for alloys forming fast-growing transient oxides or during cycling with slow heating rates. It is shown that cyclic thermogravimetry is a useful technique for quantifying the oxidation resistance of an industrial alloy. Moreover, the behaviour of the alloy is better described with CTGA than with a classic cyclic gravimetric test, because both isothermal oxidation kinetics and spalling behaviour are assessed independently. In the present case, it is shown clearly that the NiCoCrAlYTa coating greatly improves the cyclic oxidation resistance without decreasing the isothermal oxidation kinetics. Finally, the use of CTGA for performance and time-of-life evaluations is demonstrated.

Keywords: Cyclic oxidation; Kinetics; Ni alloys; MC2 alloy

1. Introduction

Structural metallic alloys are frequently subjected to combined environmental attack and mechanical stresses during their life at high temperature in industrial machines and plants. Moreover, in many industrial applications, materials experience cyclic conditions of mechanical loading, temperature and atmosphere. Under thermal cycling in an oxidizing atmosphere, chromia or alumina former alloys oxidize faster than under isothermal conditions, because spalling of the protective oxide scale leads to repeated oxidation of a bare metal surface. The consumption of alloying elements by oxidation is enhanced with the consequence of accelerated breakaway and rapid alloy microstructure evolution. In addition, alteration of

mechanical properties may result from microstructural evolution induced by alloy depletion or even from dynamic coupling between creep and oxidation [2].

The resistance of high-temperature alloys to this complex loading relies partly on their ability to form a protective oxide scale, i.e., an oxide layer with low growth kinetics and high adherence to the substrate. In order to assess quantitatively the degradation of the materials, it is then necessary to develop quantitative testing techniques. A new analysis of continuous thermogravimetry during cyclic oxidation (or cyclic thermogravimetry analysis, CTGA) [1] has been published recently. In the present work, the technique is applied to an industrial alloy: the single-crystal nickel-based superalloy MC2. Single-crystal superalloys have been developed optimizing their mechanical properties with good oxidation resistance. Nevertheless, for their application as turbine blades their oxidation and corrosion resistances are not sufficient and

* Corresponding author.

E-mail address: daniel.monceau@ensiacet.fr (D. Monceau).

they are generally coated. It is still necessary to know accurately their intrinsic oxidation resistance in case of coating cracking or spalling, and also to evaluate the time-of-life gain due to a coating.

Continuous thermogravimetry was developed for the purpose of quantification and for a more precise understanding of the mechanisms of oxidation occurring during cyclic oxidation. In 1987, Evans and Lobb [3] published an interesting study in which thermogravimetry was used to follow quantitatively the oxide scale spalling kinetics during a single cooling event. However, previous uses of thermogravimetry in thermal cyclic conditions were not quantitative [4–7], probably because of the buoyancy effect. This effect causes apparent mass changes which are not due to oxidation or spalling. The proposed recent analysis shows how the problem of buoyancy can be overcome when heating and cooling rates are high, and how it allows one to quantify independently the isothermal oxidation kinetics and the amount of oxide spalling [1]. As a consequence, the nature of the rate-controlling oxide can be monitored during the test, i.e., the occurrence of break-away and of changes in the composition or microstructure of the oxide scale can be detected. The relation between spalling and the nature of the oxide scale and its thickness can be studied, and the spalling events can also be detected. Finally, the rate of consumption of the alloying element from the matrix can be calculated as a function of the number of cycles, allowing performance evaluation and time-of-life prediction using a simple reservoir model [8], or as an input for more complex diffusion models for cyclic oxidation [9–11] which take into account the concentration gradients in the substrate.

2. Background

2.1. High-temperature oxidation of single-crystal nickel-based MC2 superalloy

Bouhanek et al. [12] have shown that the high-temperature isothermal oxidation of single-crystal nickel-based superalloys (CMSX2, CMSX4, CMSX6, AM3, MC2, SRR99) at 900, 1000 and 1100 °C in oxygen results in complex oxide-scale microstructure and large spalling during a single cooling. At 1100 °C, oxide scales are composed of alumina but with large amounts of nickel in some NiO or spinel phases formed during the transient stage of oxidation. For the MC2 alloy, these authors found a parabolic constant of $1.5 \times 10^{-6} \text{ mg}^2/\text{cm}^4/\text{s}$ at 900 °C in O₂. Using the Evans and Lobb analysis [13] of spalling during a single cooling, it was also shown that Si and Hf additions improved the resistance to spalling of the MC2 alloy.

Lasalmonie and Lautridou [14] report a comparison of oxidation kinetics in laboratory air at 1150 °C of Ni-based superalloys used in the aeronautic industry and they show that MC2 alloy has slower oxidation kinetics than IN738LC or N4 alloys but faster than CMSX4 and AM1. Previous studies of the isothermal kinetics of MC2

alloy measured at 1150 °C in flowing synthetic air [2] show a transient stage of faster kinetics during 40 min, followed by a parabolic stage with $k_p = 1.7 \times 10^{-6} \text{ mg}^2/\text{cm}^4/\text{s}$ after 7 h. It was shown also that whereas the transient kinetics was slowed down under a very low oxygen partial pressure, the decrease of k_p was very limited for the parabolic stage. These kinetics data, together with the scanning electron microscopy (SEM) coupled with energy dispersive X-ray analysis (EDX) observations of the oxide scale, are consistent with the formation of a scale of mixed oxides, but with growth kinetics controlled after a few hours at 1150 °C by a continuous alumina scale.

2.2. Previous use of continuous thermogravimetry in cyclic conditions

The usual technique to follow the kinetics of oxidation during thermal cycling consists of moving samples in and out of a regulated furnace, ideally in a controlled atmosphere, and in weighing the samples every n cycles [15]. However, this technique possesses some drawbacks including: (1) the necessity of collecting and weighing the spalls of each sample in order to measure the net mass gain and the gross mass gain simultaneously, which are both necessary to calculate independently the mass gain due to oxidation and the mass loss due to spalling; (2) the confined atmosphere around the samples in order to perform the previous task; (3) a large amount of work to prepare samples and weigh them at regular intervals, which most of the time will make it impossible to perform a measurement at each cycle; and (4) the necessity of exposing samples to ambient air and of manipulating them in order to measure their weight. For these reasons, some authors [4–7] have used a thermobalance to subject samples to thermal cycling. Recently, it has been shown that continuous thermogravimetry is a suitable technique to measure independently the oxide-scale growth kinetics and the amount of spalling at each cycle [1]. The basic principle of the analysis consists of recording the mass of the sample at the beginning and at the end of each high-temperature dwell. This technique was applied to the analysis of the cyclic oxidation kinetics of NiAl single crystals [1,16,17]. In order to perform fast heating and cooling, and to weigh simultaneously several samples independently, a new apparatus was developed and patented [18] and is now under testing. The present study was realized using a high-precision commercial thermobalance with slow heating and cooling.

3. Experimental

3.1. Sample purity and initial surface preparation

MC2 alloy is a single-crystal nickel-based superalloy, the composition of which is given in Table 1. Its microstructure consists of cuboidal γ' precipitates (L1₂) coherent with a γ (face-centred cubic) matrix. A thin sheet 1.2 mm thick was cut from a heat-treated single-crystal plate made of MC2

Table 1
Chemical composition of MC2 alloy and NiCoCrAlYTa coating

Alloy	Ni	Cr	Co	Al	Mo	Ti	W	Ta
MC2								
wt.%	Bal.	7.8	5.2	5.0	2.1	1.5	8.0	5.8
at.%	Bal.	9.1	5.3	11.2	1.3	1.9	2.6	1.9
NiCoCrAlYTa								
wt.%	Bal.	19.5	21.1	9.1	–	–	–	4.8
at.%	Bal.	20.0	19.1	18.1	–	–	–	1.4

alloy and was ground to 1 mm thickness. A 4.5×20 mm sample was then machined by spark electro-erosion. The largest surfaces were parallel to (001) lattice planes. All surfaces were mechanically polished with SiC paper and diamond paste down to 1 μm . A second specimen was coated with a 70 μm thick electrolytic NiCoCrAlYTa coating, the composition of which is given in Table 1. The coating was provided by Praxair Surface Technologies and made by the Tribomet process, where CrAlY particles are entrapped in a growing Ni–Co electroplate layer to produce a uniform dispersion. The entire surface was coated in a two-step process which leads to a slight overlap on the specimen. The sample was subjected to the usual industrial heat treatment of 6 h at 1080 °C and 20 h at 870 °C resulting in some interdiffusion between the coating and the substrate. All samples were cleaned in an ultrasonic bath with acetone followed by high-purity alcohol, before being dried. They were weighed with a 10 μg precision Sartorius balance prior to high-temperature exposure.

3.2. Thermogravimetry

Parallelepipedic samples were oxidized in a commercial Setaram TAG24s thermobalance. This apparatus combines an excellent accuracy (about 1 μg) with limited drift and buoyancy effects because of the symmetrical furnace arrangement. The difference between the mass of the oxidizing sample and the mass of an inert pure alumina reference sample placed in the symmetric furnace was recorded continuously during temperature cycling as detailed in Ref. [1]. A thermal cycle consisted of a heating period at 50 °C/min up to 1150 °C, followed by a dwell of 15 min at 1150 °C and a cooling ramp with an initial rate of 30 °C/min. This rate was maintained down to 300 °C, after which the sample was slowly cooled to 50 °C in less than 20 min and remained at a regulated 50 °C during an additional 2 min. Forty-eight identical cycles were applied to the sample in a single run. The mass was then recorded during an additional 20 h at a regulated temperature of 50 °C in order to detect a possible delayed spalling event. The total duration of one cycle was 87 min and the whole duration of the experiment was 70 h. This experiment was carried out in flowing synthetic air.

Complementary isothermal exposures were also carried out for both coated and uncoated MC2 alloy. Samples were oxidized in the same thermobalance, during 100 h at 1150 °C in flowing air (Fig. 1a).

3.3. Characterization of the morphology and microstructure of the oxide scale

Oxide scales and the underlying coating and substrate were characterized by optical microscopy and SEM using a Hitachi S3500-N instrument equipped with an Oxford Instruments 6375 EDX system for chemical analysis. The oxide phases were identified by X-ray diffraction (XRD) using a Seifert 3000TT diffractometer operated at 40 kV and 30 mA, with a constant low incidence angle of 4° in order to maximize the relative intensities of the oxide scale peaks and to get an analyzed depth that does not depend on Bragg's angle.

4. Continuous thermogravimetry measurements

4.1. Correction of the buoyancy effect

When heating and cooling the sample in the thermobalance furnace, the intensity of the Archimedes force varies because the weight of the gas changes (e.g. see Ref. [1]). This leads to an apparent mass change of the sample. This effect has probably limited the previous utilizations of thermogravimetry for cyclic oxidation studies. In Ref. [1] it was shown how this problem could be overcome. Indeed, it is possible to determine the mass of oxygen uptake during the high-temperature dwell from the measurement of mass at the beginning and at the end of the dwell. Also, because the buoyancy effect on the apparent mass of the sample is expected to be opposite and of equal intensity during heating and cooling, it is possible to determine the mass loss by spalling from the difference of the mass at the beginning of a high-temperature dwell and of the mass at the end of the preceding high-temperature dwell.

This approach makes use of the hypothesis that oxidation during heating and cooling ramps is negligible compared with the oxidation during the high-temperature dwells. This assumption is generally correct, but may lead to significant errors when fast-growing transition oxides are formed on bare surfaces after large spalling, and especially in the case of slow heating and cooling. Because the SETARAM apparatus we have used for this study does not allow fast heating and cooling rates and because an uncoated MC2 sample showed large spalling, it was decided to evaluate the amount of oxidation outside the high-temperature dwells during cyclic oxidation. It was then necessary to correct the variations of the Archimedes

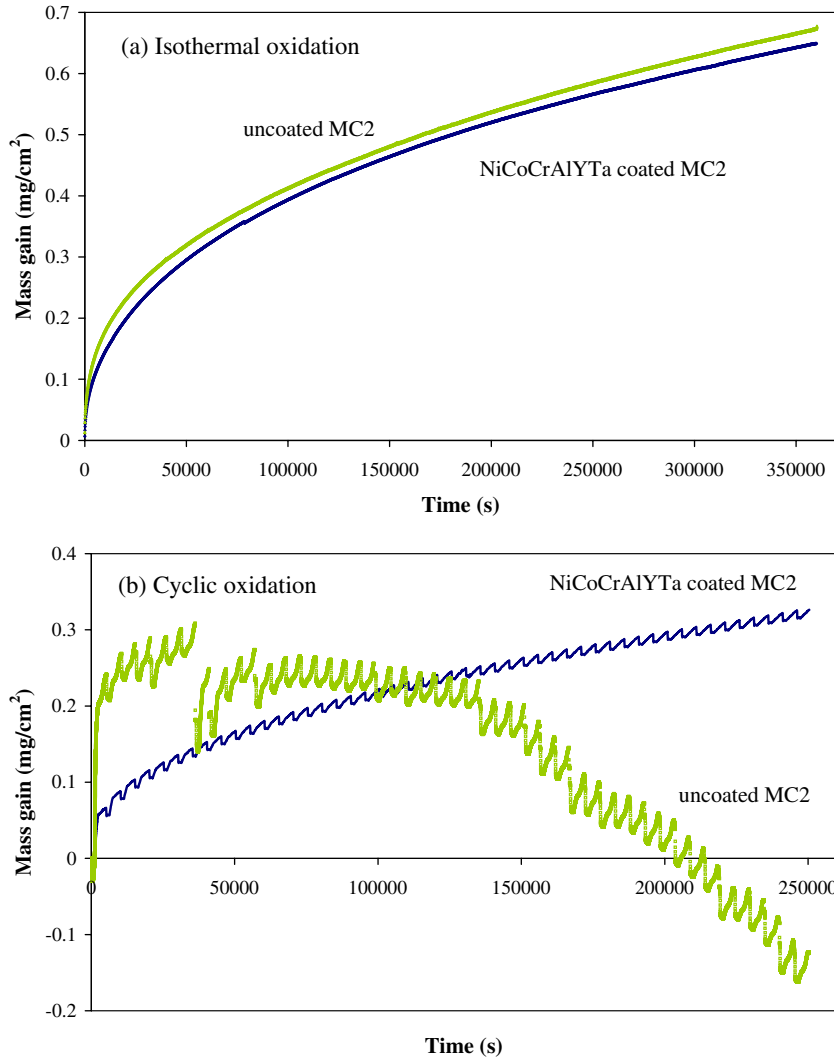


Fig. 1. Experimental mass gain of an uncoated and a coated MC2 superalloy oxidized during (a) 100 h in isothermal oxidation and (b) 48 cycles of 900 s at 1150 °C in flowing synthetic air (not corrected for buoyancy effect).

force. Fig. 1b shows the raw continuous mass recording performed during the cyclic oxidation of coated and uncoated MC2 alloy. To correct the mass variations of the MC2 sample due to the Archimedes force variations, the mass record during a cycle with negligible spalling was used (cycle 5 in our case – Fig. 2). The Archimedes equation (see Ref. [1]) was fitted on the mass curve during cooling, using the volume difference between the sample and the counterweight reference sample (symmetrical TGA) as an adjustable parameter. Cooling was preferred to heating because less oxidation is expected during cooling. Then, this fitted equation was applied to the entire mass signal, for all the cycles. The corrected mass gain from Fig. 1b is given in Figs. 3 and 4.

Fig. 4 shows the mass evolution during cycle 5, before and after correction of the buoyancy effect. This procedure has two advantages. The first is to allow the determination of the mass gain during heating and cooling periods. The second advantage of the correction is to allow an easier detection of spalling events during the cooling or heating

stages. Once the mass gain outside the high-temperature dwells has been quantified, the mass of the spalled oxide during cooling and heating can be more precisely evaluated, as shown later.

4.2. Measurement of the net mass gain during the anisotherm period preceding the high-temperature dwell n (NOD_n)

Once the recorded mass measurement has been corrected from the buoyancy effect, there are still some slight variations of the mass during the beginning of the heating ramp. These apparent variations of mass are due to slight differences in temperature between the two symmetrical furnaces of the thermobalance which are controlled by two independent regulators (right side of Fig. 4). The maximum difference of temperature between the furnaces is about 6 °C at the beginning of the heating period, leading to a “wavy” mass signal, but with small amplitude of a few micrograms only. Some variations in the gas velocity may also cause some mass variations. In total, these variations are about

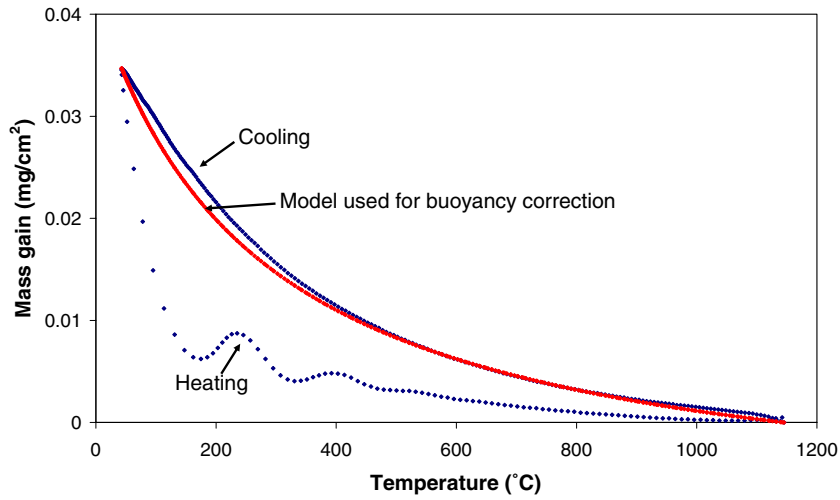


Fig. 2. Fit of the buoyancy effect during cooling of cycle 5, using the Archimedes equation. In the Setaram TAG24s thermobalance, the heating ramp shows an additional “wavy” and reproducible effect due to the difference of temperature between the two furnaces of the symmetrical arrangement. Nevertheless the overall amplitude of buoyancy effect is the same during heating and cooling.

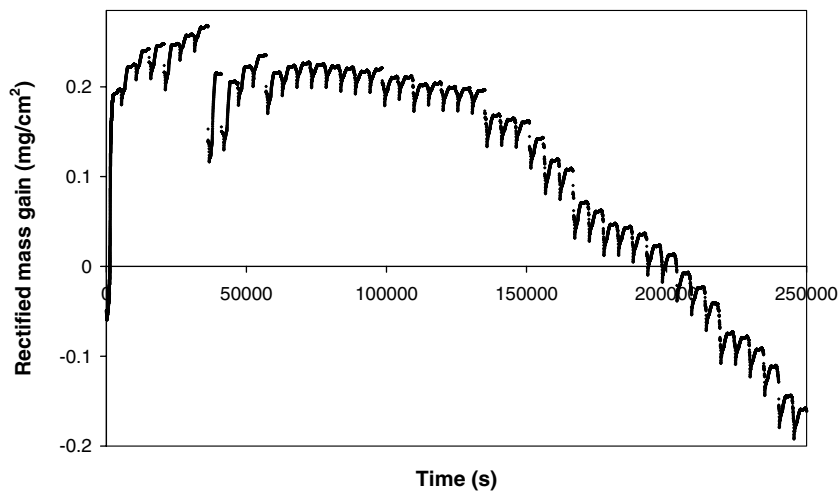


Fig. 3. Experimental mass gain for the MC2 superalloy sample oxidized 48 cycles of 900 s at 1150 °C in flowing synthetic air, after buoyancy correction.

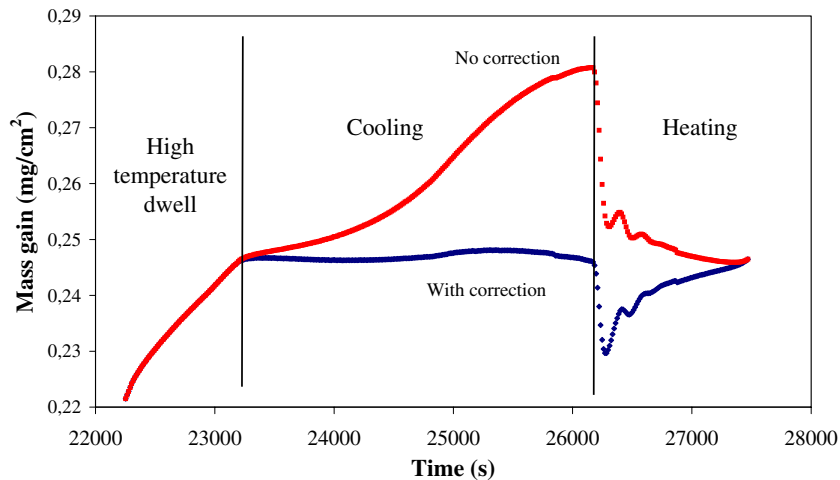


Fig. 4. MC2 sample mass variation during cycle 5 of the cyclic oxidation test (not corrected and after buoyancy correction). For this cycle, a mass gain of about 24 $\mu\text{g}/\text{cm}^2$ is recorded during the high-temperature dwell, whereas no visible spalling occurred during cooling.

10–20 μg and occur at the beginning of the heating period. When the temperature rises to about 600 $^{\circ}\text{C}$, both furnaces are at the same temperature and this effect disappears.

The actual mass increase due to oxidation during heating is only significant at the highest temperature because of the thermal activation character of oxidation kinetics. The actual mass increase during heating is also more pronounced after a large spalling during the preceding cooling. Thus, it was decided to evaluate the mass gain during the anisotherm period NOD_n (net oxygen mass gain before dwell n). After buoyancy correction, NOD_n is calculated as the mass gain during heating over 900 $^{\circ}\text{C}$ before the dwell n . NOD_n is found to be only between 0 and 5 $\mu\text{g}/\text{cm}^2$ for most cycles, with a maximum value of 20 $\mu\text{g}/\text{cm}^2$ when there is a significant spalling at the previous cooling. Despite these very small mass gains, it is worth taking into account as shown later.

4.3. Measurement of the net mass gain, spalled oxide and gross mass gain

As shown in Ref. [1], the NMG and the GMG can be easily calculated by recording only two characteristic points at each cycle: the NMG at the beginning of the high-temperature dwell $n(M_n^{\text{bg}})$ and the NMG at the end of the high-temperature dwell $n(M_n^{\text{end}})$. In the present analysis, the measurement of NMG due to oxidation during the anisotherm period preceding the high-temperature dwell n (i.e. NOD_n) allows for the correction of the calculation of the other physical parameters (see Ref. [1] for details about these parameters). The following useful data can now be calculated (per unit area of sample surface).

The variation of the net mass gain at cycle n :

$$\Delta M_n = (M_n^{\text{end}} - M_n^{\text{bg}}) + \text{NOD}_n \quad (1)$$

The mass of spalled oxide between dwell n and dwell $n + 1$ (negative value when spalling occurs):

$$\text{SOX}_n = M_{n+1}^{\text{bg}} - M_n^{\text{end}} - \text{NOD}_{n+1} \quad (2)$$

The mass of adherent oxide after n cycles:

$$\begin{aligned} \text{AOX}_n = M_{n+1}^{\text{bg}} + \left(\frac{1}{r} - 1\right) \sum_{j=1}^n (M_j^{\text{end}} - M_j^{\text{bg}} + \text{NOD}_j) \\ - M_1^{\text{bg}} + \text{NOD}_1 \end{aligned} \quad (3)$$

where r is the ratio between the mass of oxygen in the oxide and the mass of the oxide.

The gross mass gain (total amount of oxygen reacted) at the end of cycle n , after cooling:

$$\text{GMG}_n = \sum_{j=1}^n (M_j^{\text{end}} - M_j^{\text{bg}} + \text{NOD}_j) \quad (4)$$

The cumulated mass of spalled oxide at the end of n cycles:

$$\text{TOX}_n = \sum_{j=1}^n (M_{j+1}^{\text{bg}} - M_j^{\text{end}} - \text{NOD}_{j+1}) \quad (5)$$

The total NMG at cycle n , after cooling, is given by:

$$\text{NMG}_n = M_{n+1}^{\text{bg}} - \text{NOD}_{n+1} \quad (6)$$

Finally, the following equations are unchanged from Ref. [1], but the values calculated are different. The mass of metal mass consumed at cycle n :

$$\text{MET}_n = \frac{M_{\text{Met}}}{M_{\text{O}}} \text{GMG}_n \quad (7)$$

will be modified because the GMG value is corrected. The factor $M_{\text{Met}}/M_{\text{O}}$ is the ratio between the mass of metal and the mass of oxygen in the oxide, equal to $(1/r - 1)$. This ratio takes the value of 1.13 for a pure alumina former, but equals 2.55 for NiCr_2O_4 and 2.17 for Cr_2O_3 . These large differences of metal to oxygen mass ratio in oxides, together with the knowledge that an oxide scale on an industrial alloy is often a mixture of oxides, shows that this is an important possible source of error. Hence, this quantitative analysis requires an analysis of the composition of the oxide scale.

The average thickness of the oxide scale after n cycles is given by

$$e_n = \frac{\text{AOX}_n}{\rho} \quad (8)$$

where ρ is the density of the oxide. e_n is modified because the value of AOX_n has been corrected (see Eq. (3)). The value of ρ obviously depends on the nature of the oxide scale but does not vary as much as the ratio $M_{\text{Met}}/M_{\text{O}}$ ($\rho = 4.0 \text{ g}/\text{cm}^3$ for Al_2O_3 , $5.2 \text{ g}/\text{cm}^3$ for Cr_2O_3 and $5.8 \text{ g}/\text{cm}^3$ for NiCr_2O_4).

The proportion of the mass of the adherent oxide which spalls at cycle n :

$$P_n = \frac{\text{SOX}_n}{\text{AOX}_n} \quad (9)$$

will also have different values because SOX_n and AOX_n have also been corrected (Eqs. (2) and (3)).

The parabolic constant during high-temperature dwell n is still approximated by

$$k_{pn} = 2 \cdot r \cdot \text{AOX}_{n-1} \left(\frac{M_n^{\text{end}} - M_n^{\text{bg}}}{\Delta t} \right) \quad (10)$$

where r is the ratio between the mass of oxygen in the oxide and the mass of the oxide. The value of the parabolic constant is modified because AOX_n has been corrected (Eq. (3)). As explained in Ref. [1], this calculation is an approximation because it considers that the oxide scale thickness is uniform, which is not the case when spalling occurs. The error (overestimation) increases with the amount of spalling at each cycle, and this error can be evaluated using a numerical simulation [1]. For the present experiments, this error can be neglected for the coated MC2 sample and is about 10% for the uncoated MC2 when 2% of the oxide scale spalls at each cycle. Immediately after a large spalling event, this error can be larger.

4.4. Detection of the spalling events

During this study, a computer spreadsheet was developed with Microsoft Excel software in order to calculate the equations of the preceding section. In addition, an automatic procedure to detect the spalling events has been programmed. The buoyancy effect correction makes detection easier. The criterion that was used to differentiate a spalling event from noise or remaining buoyancy effect was based on a critical mass variation rate of $0.07 \mu\text{g}/\text{cm}^2/\text{s}$ during cooling and $0.5 \mu\text{g}/\text{cm}^2/\text{s}$ during heating. Therefore, it is possible to record the number of occurrences of spalling events and the temperature at which they occur.

5. Results and discussion

5.1. Isothermal oxidation

The oxidation kinetics of NiCoCrAlYTa-coated and uncoated MC2 superalloy at 1150°C are shown in Fig. 1a. These mass gains can be described as parabolic after a transient regime with slightly faster kinetics. The parabolic constants k_p were calculated by fitting a complete parabolic law $t = A + B\Delta m + (1/k_p)\Delta m^2$, where t is the time, A and B are constants and Δm is the mass variation of the sample by surface area [19]. A value of $k_p = 8.2 \times 10^{-7} \text{ mg}^2/\text{cm}^4/\text{s}$ was found for the MC2 alloy and a similar value of $k_p = 7.8 \times 10^{-7} \text{ mg}^2/\text{cm}^4/\text{s}$ was determined for the NiCoCrAlYTa-coated sample. The value for uncoated MC2 alloy is two times lower than the value measured in Ref. [2]. This is attributed to the length of the experiment (100 h here instead of 7 h for Ref. [2]) and the fact that the k_p value is still slowly decreasing after 7 h, because of the progressive formation of a protective alu-

mina subscale and because of grain growth in this scale. This is confirmed if k_p is calculated for the present data for the first 12 h (Table 3). The value of k_p for the coated alloy is five times lower than that measured in a previous study of a different sintered NiCoCrAlYTa powder after 20 h at 1150°C in dry air [20], but is in agreement with $k_p = 8 \times 10^{-7} \text{ mg}^2/\text{cm}^4/\text{s}$ measured after 18 h at 1150°C in flowing O_2 for the pure alumina former alloy NiAl(100) [1]. In conclusion, after 100 h at 1150°C in flowing synthetic air, both uncoated and coated MC2 samples have grown a protective α -alumina layer with slow isothermal oxidation kinetics. The coating does not bring any further protection to the MC2 alloy in isothermal conditions. XRD and EDS analysis confirmed that both samples formed an oxide scale consisting mainly of an α -alumina layer with a small quantity of spinel phase. In addition, uncoated MC2 seems to form a rutile-type phase but the XRD peaks were small and not well defined enough to differentiate rutile and bi- and tri-rutile phases.

Whereas coated and uncoated MC2 samples experience similar isothermal oxidation kinetics, visual observation of samples after cooling showed a large extent of spallation on the uncoated MC2 sample after 100 h at 1150°C , but no spalling on the NiCoCrAlYTa-coated sample.

5.2. Microstructural characterization of the oxide scale after cyclic oxidation

NiCoCrAlYTa-coated and uncoated MC2 superalloy samples were oxidized during 48 cycles at 1150°C in flowing synthetic air, using a 15 min hot dwell duration, i.e., a total duration of 12 h at 1150°C . An SEM image of the MC2 sample surface after cyclic oxidation is shown in Fig. 5. It can be seen from this image that spalling does not always occur at the metal/oxide interface. Most of

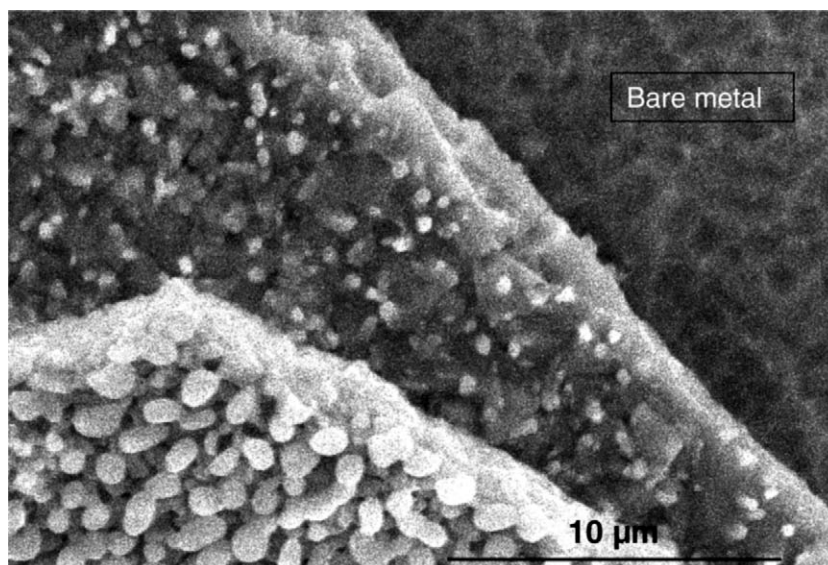


Fig. 5. SEM image of the oxidized surface of MC2 sample after 48 cycles of 15 min at 1150°C in air. Bare metal surface can be seen after spalling at metal/oxide interface. Spalling also occurs at the interface between subscales.

the time, spalling is observed inside the oxide at the interface between subscales. The fact that spalling occurs at the subscale interfaces does not influence the quantitative analysis of the continuous thermogravimetry test and even leads to a more precise calculation of the parabolic constant, which is based on the average oxide scale thickness. In the transverse view in Fig. 6, it can be seen that the oxide scale is indeed a superposition of three different layers: an alumina layer close to the metal interface, a chromium oxide layer and a spinel layer with some nickel oxide grains at the oxide/gas interface. The XRD analysis of the present uncoated MC2 sample using a fixed low incidence has confirmed that the oxide scale was composed of α -Al₂O₃, Cr₂O₃, TiO₂ or TiTaO₄ rutile, a spinel phase of the same cell parameter as NiCr₂O₄, and possibly some NiO.

Concerning the NiCoCrAlYT-Ta-coated sample, SEM observation shows almost no spalling. The XRD analysis

of the oxide scale formed after thermal cycling is identical to the XRD analysis after 100 h isothermal oxidation, i.e., the oxide scale is composed mainly of α -Al₂O₃ with some spinel phase.

5.3. Detection of spalling

Figs. 7 and 8 show the mass gain variation (corrected of the buoyancy effect) of the sample during cycles 7 and 35. The occurrence of spalling during cooling can be seen very clearly on these plots. Whereas a large spall detached from the sample at cycle 7, two smaller oxide flakes were lost at cycle 35. Analysis of all the 48 cycles shows that the spalling occurs mainly at temperatures lower than 100 °C and during cooling. But some spalling also occurs during the beginning of the heating for some cycles between cycles 30 and 36, and at each heating for cycles 36–48. There is

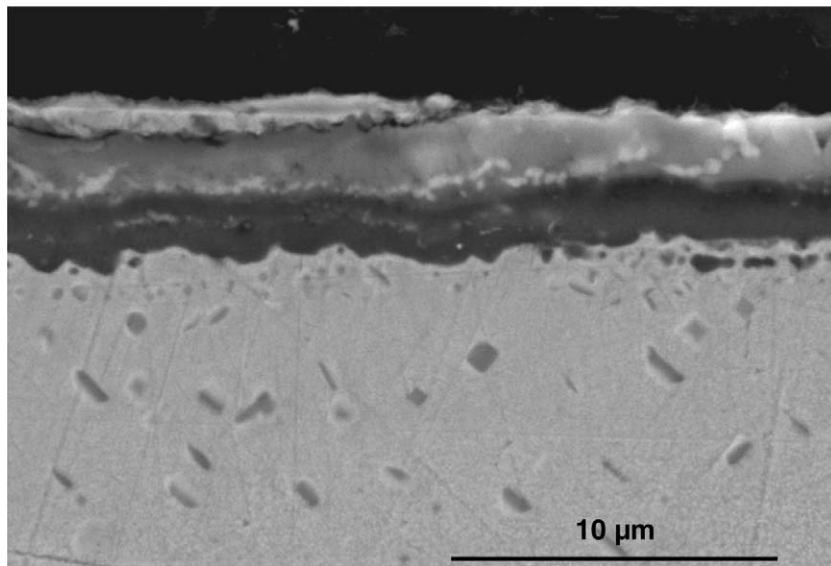


Fig. 6. SEM image of the oxidized MC2 sample cross-section. After 48 cycles of 15 min at 1150 °C in air, three oxide subscales are detected: an internal alumina layer, an intermediate chromium oxide layer and some spinel phases at the top of the scale.

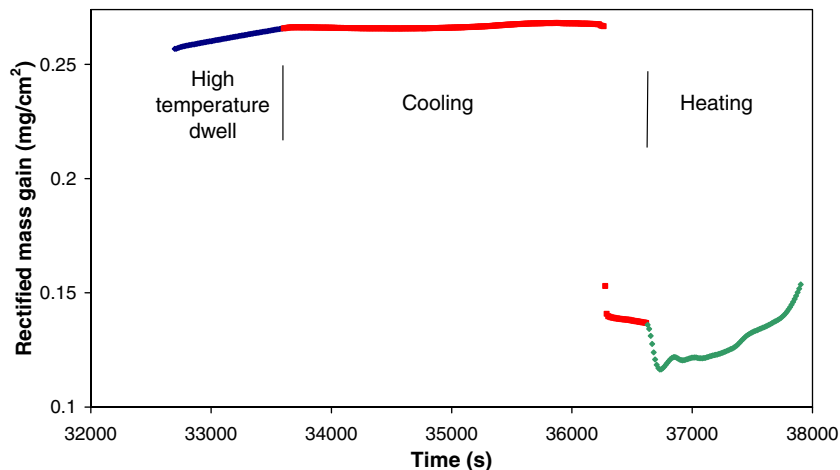


Fig. 7. MC2 sample mass variation during cycle 7 of the cyclic oxidation test (after buoyancy correction). For this cycle, a “large” mass loss of 130 μg/cm² corresponding to a single spall is recorded during cooling.

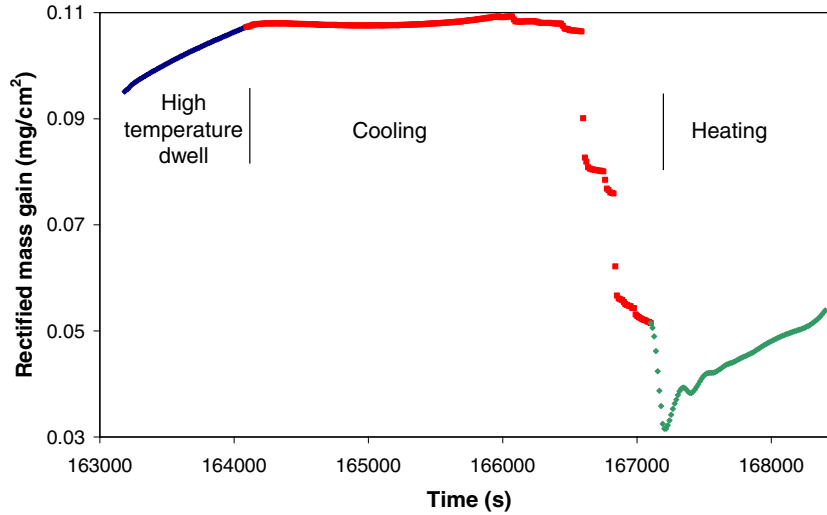


Fig. 8. MC2 sample mass variation during cycle 35 of the cyclic oxidation test (after buoyancy correction). For this cycle, at least two mass losses of about $20 \mu\text{g}/\text{cm}^2$ each are recorded during cooling, due to spalling.

also a general trend for an increasing number of spalls of decreasing mass during the progress of the experiment. This observation is surprising because one might expect the weight of each oxide spall segment to increase with time, as the average oxide scale thickness increases. Still, the total mass of the spalls is globally increasing with time.

5.4. Kinetics of cyclic oxidation

After the correction of the buoyancy effect and the calculation of the oxidation during the anisotherm periods, the different variables that characterize the kinetics of cyclic oxidation of the uncoated MC2 alloy were calculated using Eqs. (1)–(10) and are represented in Figs. 9–11. Several microstructural parameters are needed for these calculations, and they were evaluated using the XRD and SEM-

EDX analysis of the oxide scales formed on coated and uncoated MC2. For the CTGA quantification, the oxide scale formed on a NiCoCrAlYTa-coated MC2 sample is assumed to be alumina, with a density of $\rho = 4.0 \text{ g}/\text{cm}^3$ and a metal to oxygen ratio $M_{\text{Met}}/M_{\text{O}} = 1.13$. The ratio r is given by

$$r = \frac{1}{1 + \frac{M_{\text{Met}}}{M_{\text{O}}}} = 0.47$$

Concerning the uncoated MC2 sample, the oxide scale is simplified to equal volume fractions of Al_2O_3 , Cr_2O_3 and NiCr_2O_4 . Using crystallographic data to calculate the molar volume of oxygen and cations in these phases, and knowing the molar mass of these elements, the average parameters $\rho = 5.0 \text{ g}/\text{cm}^3$, $M_{\text{Met}}/M_{\text{O}} = 1.83$ and $r = 0.34$ are easily calculated for the oxide scale. Also, we can

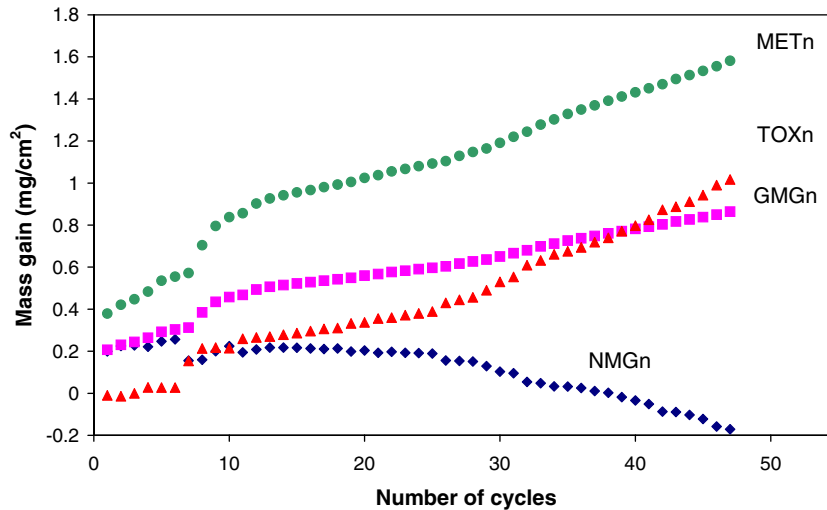


Fig. 9. Results of the CTGA of the cyclic oxidation of the MC2 superalloy, oxidized during 48 cycles of 15 min at $1150 \text{ }^\circ\text{C}$. The NMG is measured and the GMG, the TOX and the MET are calculated (see text).

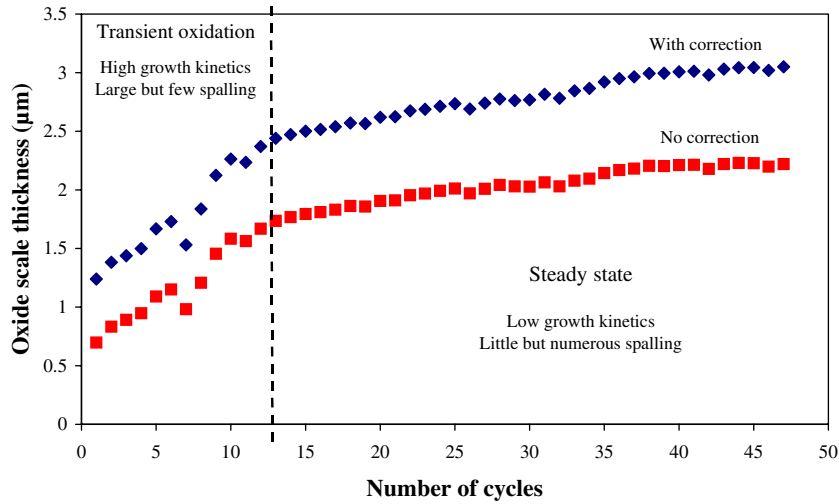


Fig. 10. Evolution of the oxide scale thickness calculated using CTGA, not corrected for buoyancy effect (square) and taking into account the oxidation during heating (diamond). After a fast growth during the first cycle (transient oxidation), the oxide scale thickness increases linearly during the first 13 cycles. Between cycles 14 and 48, the oxide scale thickness is still increasing but more slowly.

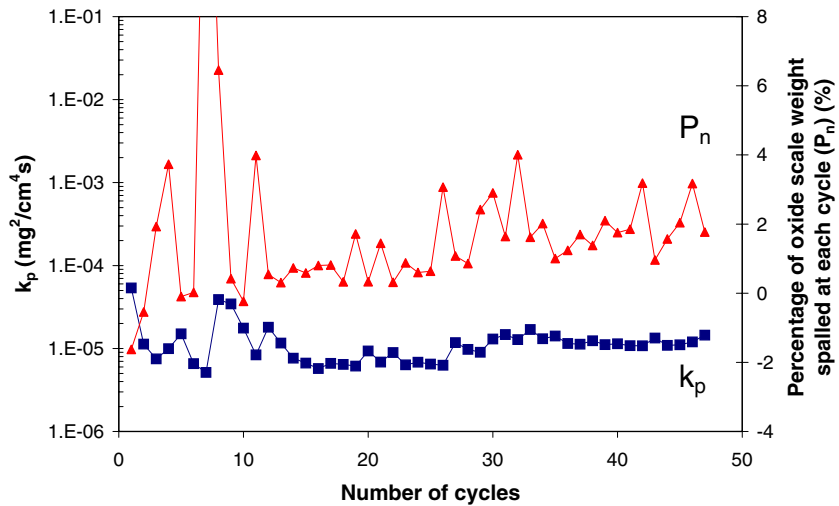


Fig. 11. Evolution of the kinetic parameters characterizing the isothermal oxidation during the high-temperature dwell (k_p) and the spalling (P_n) during cyclic oxidation of MC2 superalloy at 1150 °C.

deduce from the volume (i.e., thickness) proportions of the oxide phases in the scale that the metal consumed by cyclic oxidation is composed of 35 at.% Al, 54 at.% Cr and 11 at.% Ni, or 21 wt.% Al, 64 wt.% Cr and 15 wt.% Ni.

Fig. 9 presents the first results of the CTGA analysis for the uncoated MC2 alloy. The NMG, GMG, total mass of spalled oxide (TOX) and mass of metal consumed (MET) are given as a function of the number of cycles. MET is a particularly useful variable with which to evaluate the effect of oxidation on the alloy. First, it can be converted to a reduction of thickness of the sample, which is of engineering interest. In the present case, the cyclic oxidation of the single-crystal superalloy MC2 has consumed 1.6 mg/cm² during 48 cycles of 15 min at 1150 °C. To convert this value to a thickness, we need to take into account the composition of the metal consumed and the molar volume in

the γ phase under the scale ($V_M = 6.8 \text{ cm}^3/\text{mol}$). A value of 2.5 μm is found for the surface recession. It is of interest to note that the time evolution of MET_n is approximately linear after a transient period with a metal consumption rate of about 0.2 $\mu\text{m}/\text{h}$. In order to get a more precise analysis, it is possible to follow the time evolution of the spalling and of the oxidation kinetics.

The oxide scale thickness evolution presented in Fig. 10 is an important parameter for the mechanical modelling of the substrate/oxide composite (e.g. Ref. [21]). It was determined in the present study that the final average oxide scale thickness after 48 cycles is about 2.2 μm without the correction of the oxidation during heating, and 3.1 μm after correction, which is closer to that determined from the direct observation (Fig. 6) of the scale thickness on cross-section metallography (five random measurements over the entire

Table 2

Influence of the anisotherm oxidation correction on the evaluation of the cyclic oxidation data

	GMG ^a (mg/cm ²)	MET ^a (mg/cm ²)	TOX ^a (mg/cm ²)	AOX ^a (mg/cm ²)	<i>e</i> ^a (μm)	<i>P_n</i> ^b (%)	<i>k_p</i> ^b (mg ² /cm ⁴ /s)
No correction	0.71	1.30	0.94	1.11	2.22	2.31	8.7 × 10 ⁻⁶
With correction	0.88	1.60	1.02	1.52	3.05	1.91	10.2 × 10 ⁻⁶

^a Values calculated for the last cycle (see Fig. 9).^b Values averaged on all cycles.

sample cross-section lead to a value of 4 μm). Table 2 shows how all the calculated parameters are modified by the correction which takes into account the oxidation during heating. As stated before, NOD_{*n*} is found to be only between 0 and 5 μg/cm² for most cycles, with a maximum value of 20 μg/cm². Nevertheless, Table 2 shows that this correction should not be neglected for the present experiment.

The two key parameters to describe the cyclic oxidation kinetics are the parabolic constant *k_p*(*n*) and the proportion of the oxide scale which spalls at each cycle *P*(*n*). These two parameters are necessary to simulate the cyclic oxidation curve and to calculate useful data for engineering applications and time-of-life modelling. The parabolic coefficient *k_p*(*n*) is calculated for each high-temperature dwell with Eq. (10), and the proportion of the oxide scale which spalls at each cycle is calculated with Eq. (9). The results are shown in Fig. 11. It can be seen that the kinetics parameter *k_p*(*n*) becomes approximately constant after cycle 14, with an average value of 1.0 × 10⁻⁵ mg²/cm⁴/s between cycles 14 and 48. During the first cycles, *k_p*(*n*) values are more scattered, lying between 5 × 10⁻⁶ and 4 × 10⁻⁵ mg²/cm⁴/s. This effect may be due to the occurrence of a few large spalls during the first cycles, leading to an overestimation of *k_p* as explained before (Eq. (10)). The establishment of a stationary oxide scale microstructure may also play a role.

Concerning the spalling kinetics, it can be observed on the same graph that the proportion of the oxide scale which spalls at each cycle is slowly but continuously increasing with the number of cycles up to about 1.8% at cycle 48. During the first 14 cycles, the spalling is either low (less than 1%) or high (4–18%) for cycles 4, 7, 8 and 11. These last spalling events can be seen clearly on the NMG curve (Fig. 3). The overall kinetics of cyclic oxidation can then be modelled as a two-stage process. During the first stage (14 cycles), spalling is sparse, but when it does occur it corresponds to quite a large proportion of the scale. After cycle 14, the oxidation kinetics are almost constant.

The growth kinetics of the oxide scale are controlled by the diffusion in the alumina sublayer but chromia and spinel oxide scales are also growing and the resulting *k_p*(*n*) value is 10 times higher than for alumina formed isothermally on NiAl [16] and on the MC2 alloy. The fact that the *k_p*(*n*) value is constant during the second stage proves that the nature of the oxide scale is no longer changing much. Its higher value than for the isothermal test is consistent with the microstructure (Fig. 6). Indeed, the overall oxide scale is about three times thicker than the alumina

sublayer, and as the molar volume of oxygen in the different oxides does not vary much, a *k_p* value about nine times higher can be expected if the three scales grow together.

The gradual increase of *P*(*n*) with the number of cycles, which has been already observed in other systems including alumina formers [22] could be interpreted as an effect of the oxide scale thickness inducing an increase of the level of stress in the scale [21] or by the microstructural evolution at the oxide scale/superalloy interface. However, it should be noted that this increase is very limited and *P*(*n*) may stabilize for a longer experiment, when the average oxide scale thickness also becomes a constant, as was previously observed with NiAl [1]. This aspect of cyclic oxidation kinetics has to be considered carefully, since the time-of-life modelling of the system will be much easier if most of the life of the material is spent in a stationary regime during which the kinetic parameters are constant. Errors produced by assuming constant kinetics also need quantitative evaluation, since it was shown that the kinetic parameters can vary to a great extent, even if only alumina former alloys are considered.

5.5. Performance of the alloy in cyclic oxidation conditions and evaluation of its durability

The kinetics of spalling and of oxidation can be used for a quantitative assessment of the performance of the alloy in cyclic oxidation conditions and to evaluate its durability. It has been shown in previous works [22–25] that a “*P* – *k_p* map” is useful to give a first evaluation of the performance of a material under cyclic oxidation. As has been shown in the present study the fraction of the oxide scale which spalls at each cycle *P*(*n*) is not yet constant after 48 cycles, the kinetics of cyclic oxidation of MC2 alloy cannot be represented by a single pair of constants (*P*, *k_p*). Thus, a parametric plot (*P*(*n*), *k_p*(*n*)) with the number of cycles *n* being the variable has been plotted in the *P* – *k_p* map. The result is shown in Fig. 12, and compared in Table 3 to data obtained with the *P* – *k_p* model fitting [23] of the experimental cyclic oxidation of nickel aluminides, at the same temperature (1150 °C) but with longer dwell times (1 h). It is clearly seen that the nickel-based superalloy is lying in the alumina former zone but with faster oxidation kinetics and faster spalling kinetics than all the studied nickel aluminides, including a high-sulphur NiAl single crystal and despite shorter cycles. These data clearly demonstrate the improvement of cyclic oxidation resistance which can be obtained from the application of a nickel aluminide coating. The improvement obtained by the NiCoCrAlYTa

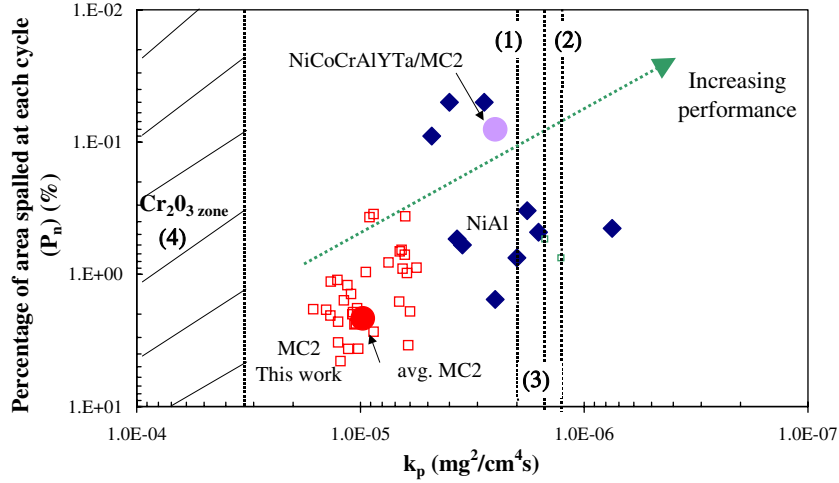


Fig. 12. “ $P - k_p$ ” map obtained for cyclic oxidation experiments at 1150 °C for alumina forming alloys: y -axis is the percentage of oxide scale spalled at each cycle (P); x -axis is the isothermal parabolic constant (k_p). MC2 superalloy (square data points represent the different values of $(P - k_p)$ for each cycle during the test) and nickel aluminides (diamond data points, see Table 2). Vertical lines refer to the isothermal oxidation kinetics of (1) NiAl [22], (2) superalloy MC2 (12 h) and (3) NiCoCrAlYTa-coated MC2 (12 h). Zone (4) refers to isothermal kinetics for chromia formers [28].

Table 3

$P - k_p$ values determined at 1150 °C in air or oxygen for various nickel aluminide alloys and for the uncoated and coated MC2 superalloy

Alloy	k_p (mg ² /cm ⁴ /s)	P_n (%)	Reference
β -NiAl undoped	1.8×10^{-6}	0.33	See Ref. [22]
Ni-10 wt.% Pt-31.5 wt.% (50 at.%) Al	2.8×10^{-6}	0.05	See Ref. [22]
Pt-50 at.% Al	4.0×10^{-6}	0.05	See Ref. [22]
Ni-51.8 at.% Al + 2.3 at.% Pt	4.8×10^{-6}	0.09	See Ref. [22]
Ni-51.2 at.% Al	1.6×10^{-6}	0.48	See Ref. [22]
Ni-47.5 at.% Al	3.7×10^{-6}	0.54	See Ref. [22]
Ni-45.1 at.% Al	2.5×10^{-6}	1.55	See Ref. [22]
Ni-44.5 at.% Al-3 ppm S	7.5×10^{-7}	0.45	See Ref. [22]
Ni-44.5 at.% Al-42 ppm S	3.5×10^{-6}	0.6	See Ref. [22]
NiAl (100)	2.0×10^{-6}	0.75	[1]
MC2 (isothermal, 7 h)	1.7×10^{-6}	–	[2]
MC2 (isothermal, 12 h)	1.3×10^{-6}	–	This work
NiCoCrAlYTa-coated MC2 (isothermal, 12 h)	1.5×10^{-6}	–	This work
MC2 (isothermal, 100 h)	8.2×10^{-7}	–	This work
NiCoCrAlYTa-coated MC2 (isothermal, 100 h)	7.8×10^{-7}	–	This work
MC2 (cyclic, 48 cycles)	1.0×10^{-5}	1.91	This work
NiCoCrAlYTa-coated MC2 (cyclic, 48 cycles)	2.5×10^{-6}	0.08	This work

coating is also clearly seen in Fig. 12. The same analysis as for the uncoated MC2, applied to the coated MC2 sample, leads to stationary cyclic oxidation kinetics $(P(n), k_p(n)) = (8 \times 10^{-2}\%, 2.5 \times 10^{-6} \text{ mg}^2/\text{cm}^4/\text{s})$. Whereas the isothermal oxidation kinetics were similar for coated and uncoated MC2 alloy, their cyclic oxidation behaviours are very different. The coated sample experiences 30 times less spalling, but also its oxidation kinetics during the high temperature dwells remains closer to the isothermal value, and then has a k_p value four times lower than the uncoated MC2 alloy. This last observation is consistent with the XRD of the oxide layer formed on the coated alloy samples which shows two identical diagrams for the isothermal and the cyclic experiments, i.e., the coated MC2 sample remains an alumina former during cyclic oxidation.

From the present analysis of the oxidation and spallation kinetics of MC2 alloy, some extrapolation can be drawn, i.e., a time-of-life prediction. For the uncoated alloy, it was shown that the kinetics can be divided in two stages. As was seen before, $k_p(n)$ remains almost constant after cycle 14 and $P(n)$ is increasing slowly together with the average scale thickness. A longer experiment would be necessary to check that $P(n)$ will reach a constant value too. Nevertheless, a first estimate of the metal consumption can be done using the present data. Averaging kinetic parameters from cycles 14–48 leads to the values $(P(n), k_p(n)) = (1.9\%, 1.0 \times 10^{-5} \text{ mg}^2/\text{cm}^4/\text{s})$. Consequently, the metal consumption can be calculated using the analytical solution presented in Ref. [23] or using a Monte Carlo simulation [26,27]. A value of 20 $\mu\text{g}/\text{cm}^2/\text{cycle}$ is found for

MET_n . This is to be added to the metal consumption during the transient stage. Finally, the metal consumption MET_n can be described by a loss of 1.6 mg/cm^2 during the 48 first cycles, followed by a stationary regime with a consumption of $0.091 \text{ mg/cm}^2/\text{h}$:

$$MET_n = 1.6 + 0.091(t - 12) \quad (11)$$

where t is the time spent at $1150 \text{ }^\circ\text{C}$, in hours.

The calculated metal consumption value can also be compared with the total Al reservoir in the 1 mm thick sample. Indeed, accelerated oxidation (“breakaway”) is expected when the alloy cannot form alumina. This thickness of 1 mm is characteristic of the size of the thin wall of some gas turbine blades used in helicopter engines. If we apply the “Al reservoir” model, i.e., if the criterion for end-of-life (EOL) is the total consumption of Al, it is possible to do a time-of-life (TOL) prediction. The total Al reservoir in the half-thickness sample is about 20 mg/cm^2 (total mass of Al in the sample divided by the surface area of the sample). We have seen previously that the Al proportion of the metal consumed was about 21 wt.%. Therefore, a maximum TOL of 1040 h can be calculated. This TOL value is a maximum because: (1) it was shown that the spalling kinetics were still increasing after 48 cycles; (2) the diffusion in the superalloy may limit the availability of Al at the metal/oxide interface; and (3) the critical content of Al at the metal/oxide interface in order to form a protective oxide layer of alumina is higher than 0 resulting also in a lower TOL. For example, a critical Al concentration of 2 at.% reduces TOL from 1040 to 842 h. To evaluate the critical Al content, it is necessary to perform a longer experiment and to record the occurrence of the large increase of $k_p(n)$ when breakaway oxidation occurs. Such an experiment necessitates the use of a specific thermo-balance with a furnace designed to sustain the necessary

number of cycles [18]. When a NiCoCrAlYTa coating is applied on MC2, the sample remains an alumina former during cyclic oxidation at $1150 \text{ }^\circ\text{C}$. Its cyclic oxidation kinetics are described by the pair of values $(P(n), k_p(n)) = (8 \times 10^{-2}\%, 2.5 \times 10^{-6} \text{ mg}^2/\text{cm}^4/\text{s})$ corresponding to a metal consumption of $MET_n = 0.016 \text{ mg/cm}^2/\text{h}$, i.e., six times lower than for the uncoated MC2 alloy. This value of MET_n can be used as a boundary condition in a diffusion model (e.g. Ref. [10]) in order to assess a TOL.

For the uncoated nickel-based superalloy MC2, another more conservative EOL criterion can be used. Indeed, the consumption of Al by cyclic oxidation causes the transformation of γ' to γ under the oxide scale. A γ phase alloy does not have the required mechanical properties for it to be used as a turbine blade. In the cross-section of Fig. 13 the γ' depleted zone can be clearly seen below the oxide scale. EDS analysis of the Al content in this γ' depleted layer shows a linear Al concentration profile between about 3 at.% under the oxide scale to about 7 at.% in the γ' depleted layer at the interface with the unchanged bulk material microstructure. A Cr depletion can be seen also, but only at some locations and only close to the oxide scale. Thus, the average Cr concentration in the depleted zone remains close to the original composition of the MC2 alloy (8 at.% instead of 9.1 at.%). Consequently, the depth Z_{dep} of the γ' depleted zone can be assumed to be controlled by the outward flux of Al. Consumption of Ni and Cr by oxidation does not much change the concentrations in the depleted zone but corresponds in part to the metal/oxide interface recession (already calculated as $2.5 \text{ } \mu\text{m}$ for 12 h and neglected here). If we equalize the mass of Al consumed by oxidation with the mass of Al released in the γ' depleted zone by the $\gamma/(\gamma + \gamma')$ interface displacement, the following relation is obtained:

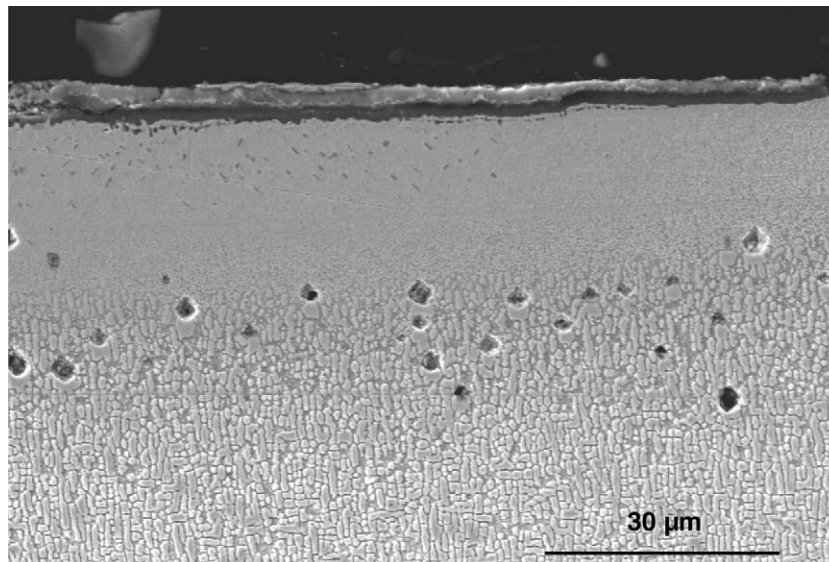


Fig. 13. Cross-section of the MC2 sample after cyclic oxidation at $1150 \text{ }^\circ\text{C}$. From top to bottom: the multilayered oxide scale, the γ' depleted layer, the γ/γ' prime bulk microstructure with faceted pores formed about $25 \text{ } \mu\text{m}$ below the surface.

$$\theta_{\text{Al}} \cdot \text{MET}_n = Z_{\text{dep}} \frac{\Delta C_{\text{Al}} M_{\text{Al}}}{V_{\text{M}}} \quad (12)$$

where θ_{Al} is the weight fraction of Al in the consumed metal MET_n , ΔC_{Al} is the difference between the Al atomic fraction in the bulk alloy and the Al average atomic fraction in the γ' depleted zone, M_{Al} is the molar mass of Al and V_{M} the molar volume in the γ phase. This leads to

$$Z_{\text{dep}}[\text{cm}] = \theta_{\text{Al}} \cdot \text{MET}_n[\text{mg}/\text{cm}^2]/244 \quad (13)$$

CTGA gives $\text{MET}_n = 1.6 \text{ mg}/\text{cm}^2$ (Table 2) corresponding to $\theta_{\text{Al}} \cdot \text{MET} = 0.34 \text{ mg}/\text{cm}^2$ of Al. Hence, the calculated growth rate of the depleted zone is about $14 \mu\text{m}$ for the first 48 cycles, i.e., about $1.2 \mu\text{m}/\text{h}$. This value has to be compared with the depth of the γ' depleted zone measured on cross-section images such as in Fig. 13. This experimental depleted zone was measured to be $20 \pm 3 \mu\text{m}$ from 10 random measurements taken in the entire sample cross-section. The prediction of the depleted layer due to cyclic oxidation is in reasonably close agreement with the observation, considering the complexity of this case with three oxide layers. More precise predictions can be expected for pure alumina or chromia formers.

It is interesting to note that this γ' depletion model leads to linear kinetics, and not parabolic, as long as the growth of the depleted layer is controlled by the constant outward flux of Al due to cyclic oxidation, and not by the diffusion in the γ' depleted zone. Using the interdiffusion coefficient in the Ni–Al system (γ phase) $\tilde{D} = 2 \times 10^{-10} \text{ cm}^2/\text{s}$ at $1100 \text{ }^\circ\text{C}$ [28], it can be verified that a $500 \mu\text{m}$ wide depletion zone, with boundary concentrations in Al of 3 and 7 at.%, is able to sustain a flux of $0.18 \text{ mg}/\text{cm}^2/\text{h}$, i.e., much greater than the required $0.34/12 = 0.028 \text{ mg}/\text{cm}^2/\text{h}$ of Al for the growth of the oxide scale.

The extrapolation of the depleted layer kinetics to the entire sample, i.e., $z_{\text{dep}} = 500 \mu\text{m}$, using the rate of $1.2 \mu\text{m}/\text{h}$ given by the CTGA, leads to a TOL of 417 h, whereas the extrapolation of the observed kinetics ($20 \mu\text{m}$ in 12 h) gives a TOL of 300 h. Of course, this value of TOL is much shorter than the 1040 h first estimated assuming the full consumption of the Al reservoir. Full γ' depletion is expected to occur before breakaway oxidation and the effect of cyclic oxidation on creep strength appears more important than chemical failure itself. This simple model allows a useful and conservative first estimation of the depletion zone thickness from the CTGA measurement. This depletion zone growth kinetics can in turn be used for a creep-based life model.

6. Conclusions

CTGA does not replace microstructural examinations of materials, but we have shown in the present work that it is an useful tool for assessing the damage due to cyclic oxidation. For a material as complex as a nickel-based superalloy, CTGA allows for the quantification of the kinetics of metal consumption due to oxidation during the high-

temperature annealing enhanced by spalling, and then allows γ' depletion layer calculation. This quantification can be used as an input in TOL models (either diffusion or creep models). Moreover, CTGA is a fast way to obtain an evaluation of the material resistance to cyclic oxidation and to compare the performance of different materials. CTGA results can be plotted in a $P(n) - k_p(n)$ parametric plot, where $P(n)$ quantifies the spalling at cycle n and $k_p(n)$ quantifies the isothermal oxidation at cycle n . Iso-TOL lines can be also plotted on this graph, when TOL is determined by alloying element loss by oxidation, depletion layer thickness or metal surface recession [21–24]. Moreover, CTGA brings additional data such as the detection of the spalling events and breakaway. Results of CTGA can be compared and checked by independent measurements, e.g. oxide scale thickness at the end of the experiment, isothermal oxidation kinetics (k_p) measured for the same alloy, mass of the collected spalled oxide flakes or metal surface recession.

Concerning the MC2 alloy studied here, CTGA and microstructural characterizations have shown that this single-crystal nickel-based superalloy is not a pure alumina former during cyclic oxidation in air at $1150 \text{ }^\circ\text{C}$. Nevertheless, it forms a continuous and compact subscale of alumina which explains the relatively low value of the parabolic constant k_p of $1.0 \times 10^{-5} \text{ mg}^2/\text{cm}^4/\text{s}$ which is more than double that for nickel aluminides (β -NiAl and Pt–NiAl) at the same temperature in cyclic conditions but much lower than for chromia formers [29]. Nevertheless MC2 alloy shows mass loss after only 40 cycles of 15 min at $1150 \text{ }^\circ\text{C}$ whereas Ni-based single-crystal René N5, which contains no Ti but 0.2 wt.% Hf, experiences mass loss after at least 500 h cycles at the same temperature [30]. This poor performance of the MC2 alloy is due to high spalling kinetics, the fraction of the oxide scale spalled at each cycle being one to two orders of magnitude higher than Pt-modified β -nickel aluminides and also higher than the electrolytic NiCoCr–AlYTa coating tested in the present study. This emphasizes the fact that the main way by which this alloy can be improved is by an increase in the mechanical stability of its oxide scale, if this material is to be used uncoated.

Acknowledgement

The comments and inputs of James L. Smialek (NASA Glenn Research Center) are gratefully acknowledged.

References

- [1] Monceau D, Poquillon D. *Oxid Met* 2004;61:143–63.
- [2] Dreyepont S, Monceau D, Crabos F, Andrieu E. *Acta Mater* 2005;53:4199–209.
- [3] Evans HE, Lobb RC. *Proc Eurocorr* 1987;87:135–40.
- [4] P. Moulin, PhD thesis, University Paris Sud; 1978.
- [5] Pivin JC, Delaunay D, Roques-Carmes C, Huntz AM, Lacombe P. *Corros Sci* 1980;20:351–73.
- [6] Vangeli P, Ivarsson B. *Mater Sci Forum* 2001;369–372:785–92.
- [7] Krupp U, Chang SY, Schimke A, Christ HJ. In: Schütze M, Quadackers WJ, Nicholls JR, editors. *Lifetime modelling of high*

- temperature corrosion processes, EFC 34. London: Maney Publishing. p. 148–64.
- [8] Nicholls JR, Newton R, Bennet MJ, Evans HE, Al-Badairy H, Tatlock GJ, Naumenko D, Quadackers J, Strehl G, Borchardt G. In: Schütze M, Quadackers WJ, Nicholls JR, editors. Lifetime modelling of high temperature corrosion processes, 34. London: Maney Publishing; 2001. p. 83–106.
- [9] Nesbitt JA, Heckel RW. *Thin Solid Films* 1984;119:281–90.
- [10] Nesbitt JA. *Oxid Met* 1995;44:309–38.
- [11] Bacos MP, Josso P, Vialas N, Poquillon D, Pieraggi B, Monceau D, Nicholls JR, Simms N, Encinas-Oropesa A, Ericsson T, Stekovic S. *Appl Therm Eng* 2004;24:1745–53.
- [12] Bouhanek K, Oquab D, Pieraggi B. *Mater Sci Forum* 1997;251–254:33–40.
- [13] Evans HE, Lobb RC. *Corros Sci* 1984;24:209–22.
- [14] Lasalmonie A, Lautridou JC. In: Huntz AM, Pieraggi B, editors. *Oxydation des matériaux métalliques*, Paris Lavoisier; 2003. p. 367–88.
- [15] in http://cotest.dechema.de/Code_of_Practice.html (2005).
- [16] Poquillon D, Oquab D, Viguier B, Senocq F, Monceau D. *Mater Sci Eng A* 2004;381:237–48.
- [17] Poquillon D, Oquab D, Monceau D. *Mater Sci Forum* 2004;461–464:737–45.
- [18] Salabura JC, Monceau D. *Mater Sci Forum* 2004;461–464:689–96.
- [19] Monceau D, Pieraggi B. *Oxid Met* 1998;50:477–93.
- [20] Juarez F, Monceau D, Tetard D, Pieraggi B, Vahlas C. *Surf Coat Technol* 2003;163–164:44–9.
- [21] Evans HE. *Int Mater Rev* 1995;40:1–40.
- [22] Vialas N, Monceau D, Pieraggi B. *Mater Sci Forum* 2004;461–464:747–54.
- [23] Poquillon D, Monceau D. *Oxid Met* 2003;59:409–31.
- [24] Poquillon D, Monceau D. In: *Proceedings of the TMS annual meeting, San Diego*; 2003. p. 165–72.
- [25] Smialek J. *Acta Mater* 2004;52:2111–21.
- [26] Lowell CE, Barrett CA, Palmer RW, Auping JV, Probst HB. *Oxid Met* 1991;36:81–112.
- [27] Monceau D, Communication at Journées d’automne de la Société Française de Métallurgie (SF2M), Paris; 2000.
- [28] Watanabe M, Horita Z, Smith DJ, McCarney MR, Sano T, Nemoto M. *Acta Metall Mater* 1994;42:3389–96.
- [29] Hindam H, Whittle DP. *Oxid Met* 1982;18:245–84.
- [30] Smialek J, Pint B. *Mater Sci Forum* 2001;369–372:459–66.